CHEMISTRY OF MATERIALS

ARTICLE

pubs.acs.org/cm

Synthesis, Structure and Properties of Several New Oxychalcogenide Materials with the General Formula $A_2O_2M_2OSe_2$ (A = La−Sm, M = Fe, Mn)

David G. Free, Neil D. Withers, Peter J. Hickey, and John S. O. Evans*

Department of Chemistry, Durham University, Durham, United Kingdom, DH1 3LE

Supporting Information

ABSTRACT: We report the synthesis of a series of manganese-containing oxychalcogenides with general formula $A_2O_2Mn_2OSe_2$ (A = La, Ce, Pr) as well several new $A_2O_2Fe_2OSe_2$ materials (A = La−Sm). We report the structural, magnetic, and conduction properties of the manganese-containing materials: $La_2O_2Mn_2OSe_2$, $Ce_2O_2Mn_2OSe_2$, and $Pr_2O_2Mn_2OSe_2$. These materials are isostructural with $La_2O_2Fe_2OSe_2$, and are shown to undergo a phase transition on cooling, apparently related to displacement of oxide ions from the $[Mn_2O]^{2+}$ plane. Peak splitting has been observed in the Pr^{3+} containing material at low temperatures, consistent with a reduction to orthorhombic symmetry. All of the manganese containing materials order antiferromagnetically on cooling with $\boldsymbol{k}$ = (0, 0, 0), T_N = 164−184 K, and have a 12 K Mn^{2+} moment of around 4 μ_B. The magnetic structure of $La_2O_2Co_2OSe_2$ is also reported. Conductivity studies have shown that $La_2O_2Mn_2OSe_2$ and $La_2O_2Co_2OSe_2$ are both semiconducting, with activation energies of ∼0.24 and 0.35 eV.

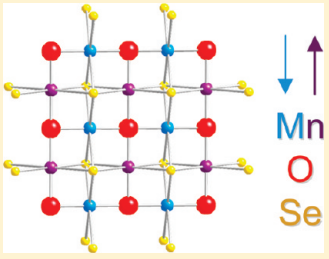

KEYWORDS: characterization of materials, inorganic solids and ceramics, magnetic materials

INTRODUCTION

Since the discovery of high-temperature superconductivity in layered oxypnictides and iron selenide, there has been significant interest in mixed anion materials.[1−7] The electronic properties of the superconducting phases are associated with layers of edge-sharing FeX_4 (X = chalcogenide, pnictide) tetrahedra which produce a square array of Fe sites with an Fe−Fe edge of ∼2.8 Å. These materials are generally poor metals which order to a variety of antiferromagnetic (AFM) structures on cooling (often associated with symmetry-reducing phase transitions) and can be electron or hole doped into the superconducting state. There have been several reviews on the properties of these materials including those by Ozawa & Kauzlarich, Paglione & Greene, and Johnston.[7−9]

There have been a number of recent publications on materials related to $La_2O_2Fe_2OSe_2$, the synthesis and structure of which was originally reported by Mayer et al.[10,11] These materials formally contain the same ∼2.8 Å square array of Fe sites but with an additional oxygen for every two Fe atoms. The presence of this additional oxygen ion means that Fe−Fe distances are ∼6% larger than in FeSe/FeTe, and ∼1% larger than in LaOFeAs, and band structure calculations reveal a narrower band such that $La_2O_2Fe_2OQ_2$ are Mott-insulators.[12] The $La_2O_2Fe_2OSe_2$ structure type is shown in Figure 1a and consists of layers of edge-sharing La_4O tetrahedra separated from anti-CuO_2 type $[Fe_2O]^{2+}$ layers by a layer of Se^{2-} ions. The Se^{2-} ions are arranged such that the coordination geometry of the transition metal is a distorted octahedron, with two axial oxide ions and four equatorial selenide ions; transition metal octahedra then share faces with adjacent octahedra. Despite the different transition metal coordination environment, we can develop a relatively straightforward relationship between this structure and the more familiar ZrCuSiAs structure, adopted by the "1111" pnictide super conductors, LaOFeAs, and oxychalcogenides such as $AOCuQ$ (Q = S, Se, Te).[13] When Se^{2-} is substituted for As^{3-} in LaOFeAs charge compensation can be achieved in a number of ways: in isostructural LaOCuSe one has formally Cu^{1+} present; for transition metals which remain formally M^{2+} (Mn^{2+}, Fe^{2+} & Cd^{2+}) one can form $AOM_{0.5}Se$ ($A_2O_2MSe_2$) materials, Figure 1b, containing either ordered, or disordered metal vacancies;[14−16] in the title compounds, which retain a 1:1 A:M ratio, charge balance is achieved by introduction of the extra oxygen into the square-planar transition metal layers. In LaOCuSe one has pairs of Se^{2-} ions, above and below the transition metal layer, at 90° to each other when viewed down the c axis, giving tetrahedral transition metal coordination. On can conceptually imagine rotating one pair by 90° as the oxygen is introduced to give the octahedral MSe_4O_2 coordination observed in $La_2O_2M_2OSe_2$.

This close structural relationship, and in particular the similar transition metal lattice in the title and 1:1:1:1 phases, makes this a fascinating system, particularly if materials could be doped to become conducting. Known materials with this structure type have recently been expanded to include $La_2O_2Co_2OSe_2$, $Nd_2O_2Fe_2OSe_2$ and $Sm_2O_2Ti_2OSb_2$;[17−20] since this work was completed, two reports on $La_2O_2Mn_2OSe_2$ have appeared.[22,23] We have recently reported the low-temperature structural properties of $La_2O_2Fe_2OSe_2$ and $La_2O_2Fe_2OS_2$ revealing them to have frustrated magnetic structures different from those that had been

Received: December 13, 2010
Revised: January 31, 2011
Published: February 28, 2011

dx.doi.org/10.1021/cm1035453 | *Chem. Mater.* 2011, 23, 1625–1635

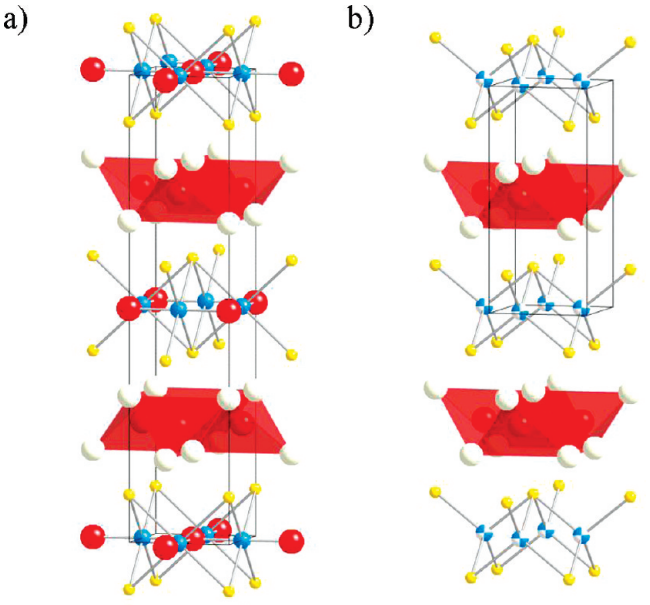

Figure 1. $La_2O_2Fe_2OSe_2$ structure type adopted by (a) $Ce_2O_2Mn_2OSe_2$ and the ZrCuSiAs structure of (b) $CeOMn_{0.5}Se$; Ce^{3+} = white, O = red, Se = yellow, Mn^{2+} = blue; in (b) the Mn^{2+} sites are half occupied.

predicted but similar to that of FeTe.[12,21] To give better understanding of the structural and physical properties of these systems and explore the electronic and magnetic properties of the unusual anti-CuO_2 M_2O layers we have investigated the range of stability of this structure type for different rare-earth and transition metals, which we report here. We have prepared a range of materials with the general formula $A_2O_2Mn_2OSe_2$ (A = La, Ce, Pr) and report their structure, phase transitions and low temperature magnetic structures. We have also extended the range of known Fe-containing materials to include La−Sm and confirm the magnetic structure of $La_2O_2Co_2OSe_2$ as proposed by Fuwa et al.[20]

EXPERIMENTAL SECTION

$A_2O_2M_2OSe_2$ materials were prepared using two differing techniques. In the case of La and Pr containing materials, stoichiometric amounts of A_2O_3 (La_2O_3 Sigma-Aldrich 99.9%; Pr_2O_3 was prepared by reduction of Pr_6O_{11} under vacuum at 1000 °C, Sigma-Aldrich 99.9%), Mn (Sigma-Aldrich, 99.99%), Fe (Aldrich, 99.9%), Co (Alfa-Aesar. 99.8%) and Se (Alfa-Aesar, 99.999%) were ground together and pressed into a 5 mm pellet. This was placed inside a 7 mm diameter high density alumina crucible and sealed in a quartz ampule under vacuum. For the Ce-containing material, stoichiometric amounts of CeO_2 (Alfa-Aesar, 99.99%), Mn or Fe, and Se were used in the synthesis, and an Al (Alfa-Aesar, 99.5%) containing crucible was included in the quartz ampule to remove excess oxygen released during the reaction. In both cases the quartz ampule was heated with the following routine: ramp to 600 °C at 1° min^{-1} and dwell for 12 h, ramp to 800 °C at 0.5° min^{-1} and dwell for 1 h, ramp to 1000 °C at 1° min^{-1}, and dwell for 12 h. After this the furnace was allowed to cool to room temperature. Analysis of the products by powder X-ray diffraction confirmed that the target phase had been obtained. The manganese-containing samples were all olive-green in color, the iron-containing materials were black and the cobalt-containing material gray.

Neutron powder diffraction data for structural analysis of the manganese series of materials were collected using the high resolution diffractometer (HRPD) at ISIS over a time-of-flight (TOF) window of 10−210 ms (d = 0.2−16.4 Å) at 12 and 300K, with the sample mounted in a 5 mm vanadium slab can for a total of 66 μAh. X-ray data were collected at the same temperatures using a Bruker d8 Advance diffractometer, with a LynxEye silicon strip detector, from 5 to 120° 2θ with a step size of 0.021° and collection time of 8 s per step; sample temperature was controlled using an Oxford Cryosystems PheniX CCR cryostat. Data were analyzed over TOF ranges of 15−200 ms for each of two neutron banks (backscattering (bs) and 90°), and 20−120° 2θ for the X-ray data. Combined X-ray and neutron refinements were performed in TOPAS Academic for the 300 and 12 K data collections.[24] Parameters refined at 12 and 300 K included those listed in Table 2, as well as parameters to model the background, TOF and X-ray instrument calibration, absorption, scale factors and profile coefficients. The overall number of variables refined for each fit are stated in Table 2. Rapid variable-temperature data were also collected at HRPD in 6 K intervals, from 12 to 300 K, for 2.5 μAh. Room temperature X-ray data were collected under similar conditions for the iron materials. Neutron data for $La_2O_2Co_2OSe_2$ were collected at 12 K on SEPD at the IPNS facility in Argonne, and data from the 145°, 90° and 44° banks were used in analysis. Magnetic structures were determined uing SARAh Refine, interfaced with GSAS.[25,26] Final refinements were performed using either a Shubnikov or distortion mode approach within TOPAS Academic.[24] Final refinements were checked in GSAS for consistency. Variable temperature data were analyzed using the SEQGSAS routine in GSAS, and in TOPAS Academic using the local program multitopas.

Table 1. Lattice Parameters for $A_2O_2M_2OSe_2$ Materials, with M = Co, Fe, Mn

$A_2O_2M_2OSe_2$	a (Å)	c (Å)	V (Å)^3	c/a
$La_2O_2Co_2OSe_2$[17]	4.0967(1)	18.4198(2)	306.52(3)	4.4963(1)
$La_2O_2Fe_2OSe_2$[11]	4.084466(9)	18.59798(7)	310.268(2)	4.55334(2)
$Ce_2O_2Fe_2OSe_2$	4.05928(9)	18.4638(5)	304.24(1)	4.5485(2)
$Pr_2O_2Fe_2OSe_2$	4.04351(4)	18.4476(3)	301.618(6)	4.56227(9)
$Nd_2O_2Fe_2OSe_2$[20]	4.0263(1)	18.4306(2)	298.7676	4.5776(1)
$Sm_2O_2Fe_2OSe_2$	4.00079(7)	18.3827(5)	294.24(1)	4.5948(1)
$La_2O_2Mn_2OSe_2$	4.138921(4)	18.84990(3)	322.911(1)	4.55430(1)
$Ce_2O_2Mn_2OSe_2$	4.11304(2)	18.74100(9)	317.043(3)	4.55648(3)
$Pr_2O_2Mn_2OSe_2$	4.09739(2)	18.69481(9)	313.860(3)	4.56261(3)

Synthesis of a large pure sample of $Ce_2O_2Mn_2OSe_2$ for neutron diffraction was difficult and impurity phases were also included in the refinement. These included MnSe (∼1%), CeO_2 (∼1%), $CeOMn_{0.5}Se$ (∼2%) and an unknown phase (10−15%) with peak positions and intensities suggesting a structure closely related to the target phase; numbers in brackets are approximate weight fractions. The similarity in the structures of $Ce_2O_2Mn_2OSe_2$ and $CeOMn_{0.5}Se$ suggests that the unknown phase observed could contain defects related to the latter structure in the former.

Resistivity data were recorded for $La_2O_2Mn_2OSe_2$ and $La_2O_2Co_2OSe_2$ using a Keithley Instruments electrometer, with the sample cooled via an Oxford Instruments cryostat and temperature controller. Samples were prepared as 5 mm pellets ($La_2O_2Mn_2OSe_2$ = 0.80 mm and $La_2O_2Co_2OSe_2$ = 0.60 mm thick) and the faces coated with a layer of gold followed by silver paint. The samples were cooled and warmed, between 300 and 80 K, with data collected in 5 K increments.

Magnetic susceptibility data were collected using a Magnetic Properties Measurement System (Quantum Design, MPMS). Field cooled and zero-field cooled data were recorded from 2 to 292 K, in 5 K temperature increments, in a field of 100 Oe. Hysteresis measurements were taken at room temperature from 0 to 2 T, and at 12 K between −2 and 2 T.

RESULTS AND DISCUSSION

We have prepared eight new materials in the $A_2O_2M_2OSe_2$ family, as summarized in Table 1 and Figure 2, although the

dx.doi.org/10.1021/cm1035453 |Chem. Mater. 2011, 23, 1625–1635

Table 2. Results from Combined X-ray/Neutron Rietveld Refinements of $A_2O_2Mn_2OSe_2$ Materials at 295 and 12 K[a]

$A_2O_2Mn_2OSe_2$	A = La		A = Ce		A = Pr	
T (K)	295	12	295	12	295	12
space/Shubnikov group	$I4/mmm$	$I4'/mm'm$	$I4/mmm$	$I4'/mm'm$	$I4/mmm$	$Im'm'm$
a (Å)	4.138921(4)	4.12870(1)	4.11304(2)	4.10247(1)	4.09739(2)	4.08616(3)
b (Å)	= a	= a	= a	= a	= a	4.09417(4)
c (Å)	18.84990(3)	18.78115(5)	18.7410(9)	18.70183(8)	18.69481(9)	18.5539(1)
V (Å^3)	322.911(1)	320.146(1)	317.043(3)	314.757(2)	313.859(3)	309.789(6)
A_z	0.18668(1)	0.18644(1)	0.18725(3)	0.18700(2)	0.18843(2)	0.18826(3)
Sez	0.09994(2)	0.09999(2)	0.10118(3)	0.10089(3)	0.10164(3)	0.10167(3)
O(1) z	0.25	0.25	0.25	0.25	0.25	0.2512(2)
Mn M_z (μ_B)		4.223(7)		4.023(7)		4.219(8)
A U_{eq} (100 × Å^2)	1.007(8)	0.51(1)	0.84(2)	0.49(2)	1.00(2)	0.71(3)
Mn(1) U_{eq} (100 × Å^2)	1.63(2)	0.63(2)	1.39(3)	0.63(2)	1.58(2)	0.28(7)
Mn(2) U_{eq} (100 × Å^2)						2.1(1)
Se U_{eq} (100 × Å^2)	1.24(1)	0.68(1)	1.13(1)	0.70(1)	1.30(1)	1.34(3)
O(1) U_{eq} (100 × Å^2)	1.01(2)	0.58(1)	0.92(2)	0.68(2)	0.94(1)	0.90(3)
O(2) U_{eq} (100 × Å^2)	3.07(3)	2.82(3)	3.37(4)	2.49(3)	3.71(3)	5.35(7)
R_{wp} (%)	3.52	4.11	3.58	3.93	3.37	4.94
χ^2	4.51	4.52	3.67	4.38	3.07	4.61
no. of variables	70	70	91[b]	91[b]	68	78

[a] U_{ij} values are given in the Supporting Information. [b] Includes parameters used to model impurity phases.

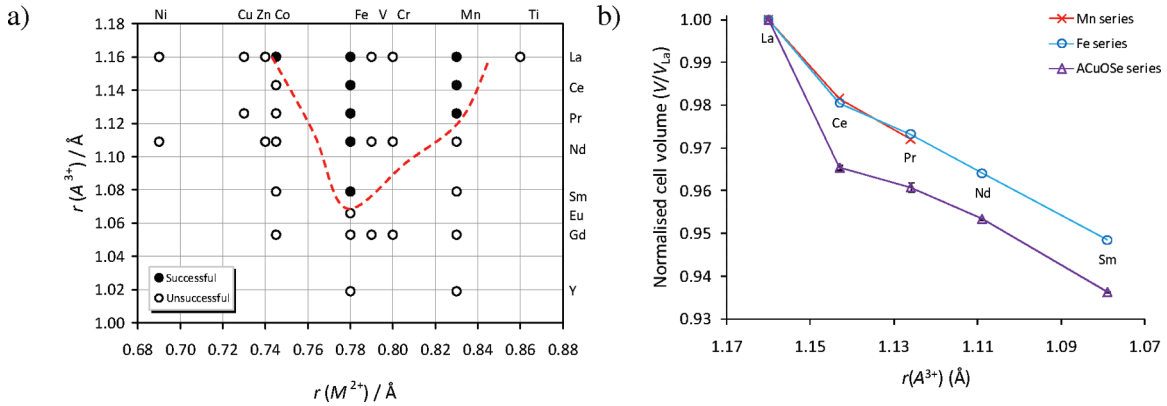

Figure 2. (a) Materials successfully prepared (filled circles) and (b) the effect of decreasing lanthanide radius on the cell volume of $A_2O_2M_2OSe_2$ (M = Mn, Fe) and AOCuSe;[28,29] the dashed line in panel a is a guide to the eye.

syntheses of $La_2O_2Co_2OSe_2$, $Ce_2O_2Fe_2OSe_2$, and $Nd_2O_2Fe_2OSe_2$ have recently been reported elsewhere.[17,19,20] For M = Fe, A = La—Sm phases are stable and for M = Mn A = La—Pr; lattice parameters are given in Table 1. Figure 2a gives a summary of both successful (black circles) and unsuccessful (white circles) syntheses plotted relative to the radii of the cations involved (transition metal radii used are the high spin radii reported by Shannon).[27] For V and Cr, phases containing higher transition metal oxidation states were formed as expected. The $La_2O_2Fe_2OSe_2$ structure-type is thermodynamically stable for M = Mn, Co and Fe, with iron-containing materials forming for the widest range of rare-earth radii. This presumably reflects an optimum size match between the $[FeO_2Se_4]^{2-}$ and $[A_2O_2]^{2+}$ layers. It is notable from Table 1 that while overall cell volumes for the lanthanum-containing materials show the expected decrease with the size of M^{2+}, there is a significant change in c/a ratio between the materials. This reflects changes in the various slabs of the structure. As the transition metal radius decreases from Mn^{2+} to Co^{2+} there is a significant decrease in the height of the M_2OSe_2 slabs which is only partially compensated by an increase in the height of the A_4O slabs, leading to a reduction in c/a.

In syntheses where the target phase was not obtained, a variety of other phases was formed. In most cases these were lanthanide-oxide starting material plus the transition metal monoselenide. For reactions with smaller lanthanides, particularly those involving manganese, A_2O_2Se was formed, alongside MSe and MO. For the late transition metals the formation of ZrCuSiAs-related materials, such as LaOCuSe, was observed. Presumably the high stability of these phases prevents the formation of the $A_2O_2M_2OSe_2$ structure under thermodynamic control. In the case of vanadium and chromium the phase mixture formed was driven by the formation of stable M^{3+} perovskite phases $LaVO_3$ and $LaCrO_3$. Several unknown phases were also observed, especially for syntheses involving vanadium, chromium, or titanium. There are, however, several 3-dimensional oxychalcogenides known to exist containing these metals.

dx.doi.org/10.1021/cm1035453 |Chem. Mater. 2011, 23, 1625–1635

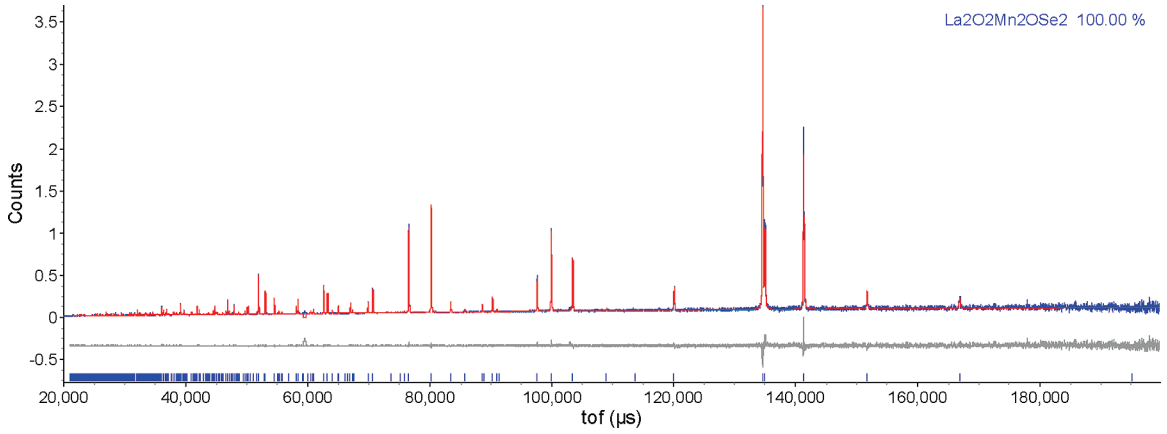

Figure 3. Rietveld refinement results for $La_2O_2Mn_2OSe_2$; data shown are from the HRPD backscattering bank (the observed pattern is blue, calculated in red and the difference in gray). Tick marks show predicted peak positions. The *d*-spacing range shown is ∼0.4−4 Å.

Figure 2b shows the variation in cell volume across the $A_2O_2Mn_2OSe_2$ and $A_2O_2Fe_2OSe_2$ series, with the trend for *A*OCuSe phases included for comparison.[28,29] We observe the expected decrease in cell volume as the lanthanide radius decreases. There is an indication that the La member is slightly larger than expected from other members of the series. A similar effect is observed in the *A*OCuSe materials and also in lanthanide monophopshides.[30] The larger volume observed for the La-containing materials derives principally from a larger *c* cell parameter, reflected by an increase in the separation of the $[A_2O_2]^{2+}$ and $[MO_2Se_4]^{2-}$ layers.

■ VARIABLE TEMPERATURE STRUCTURAL STUDIES OF $A_2O_2Mn_2OSe_2$

High quality X-ray (XRD) and neutron diffraction (ND) data were collected on the Mn^{2+} containing materials at 300 and 12 K. Results of Rietveld refinement for *A* = La confirm the material is isostructural with $La_2O_2Fe_2OSe_2$; coordinates are given in Table 2 and a Rietveld plot for backscattering 300 K data is given in Figure 3; Rietveld fits for each bank of data at 300 and 12 K are given in the Supporting Information along with those for Ce and Pr phases. When site occupancies were refined for $La_2O_2Mn_2OSe_2$ and $Pr_2O_2Mn_2OSe_2$, with the *A* site occupancy fixed at 1.0 to provide an overall scale, they refined to values within three standard uncertainties of 1.0, suggesting a stoichiometric material within the limits of the diffraction data: $La_2O_{1.988(4)}Mn_{2.001(4)}O_{0.993(4)}Se_{2.009(3)}$, and $Pr_2O_{2.006(5)}Mn_{2.000(6)}O_{1.003(4)}Se_{2.006(5)}$. For $Ce_2O_2Mn_2OSe_2$, the refined composition was $Ce_2O_{2.030(6)}Mn_{1.994(6)}O_{1.040(5)}Se_{1.993(5)}$, though the quality of the diffraction data is lower than for the other materials. Although this is close to the stoichiometry expected for Ce^{3+} and Mn^{2+}, we cannot exclude the possibility of partial oxidation of cerium. Similar to recent observations on $La_2O_2Fe_2OSe_2$, the thermal displacement of the O(2) ion (in the $[M_2O]^{2+}$ layers) at both temperatures is significantly higher than those of other sites.[11] An anisotropic refinement model shows that the main contribution to this is from the U_{33} parameter, suggesting that the O(2) ion is displaced from the $[Mn_2O]^{2+}$ layer; i.e. that there is a local out of plane static or dynamic deviation of the Mn−O−Mn bond away from 180°. Similar effects were observed for *A* = Pr, though were less marked for *A* = Ce.

Figures 4a−c show cell parameters and unit-cell volume for $La_2O_2Mn_2OSe_2$, $Ce_2O_2Mn_2OSe_2$, and $Pr_2O_2Mn_2OSe_2$ extracted from neutron data collected between 12 and 300 K; a plot of *c*/*a* ratio as a function of temperature is given in the Supporting Information. These data show a marked change in thermal expansion of the *c* axis for each material at ∼115, 90, and 180 K, respectively. This change is similar to, although more marked than, that reported for $La_2O_2Fe_2OSe_2$.[11] The temperature of the transition and the magnitude of the change in thermal expansion for these materials do not show a simple correlation with the size of the rare-earth ion. This could be due to partial oxidation of the cerium ion in $Ce_2O_2Mn_2OSe_2$ from Ce^{3+} to Ce^{4+}, as has been observed in CeOCuS; however, Figure 2b suggests that there is no significant anomaly in the size of the unit cell at room temperature.[31−33] Similarly, the more marked effect observed for $Pr_2O_2Mn_2OSe_2$ could be related to the low temperature structural transition, discussed below. In each material the phase transition on cooling is accompanied by an increase in the U_{33} displacement parameter of the O(2) ion (Figure 4d). As discussed above, this could be consistent with a static displacement of the O(2) ion out of the $[Mn_2O]^{2+}$ plane at low temperature. This effect is most marked for the praseodymium containing material reflecting the larger effect seen in the *c* cell parameter. Refinement using a split site for O(2) in the Pr material gave U_{33} values only slightly higher than those of other ions and an O(2) displacement from the $[Mn_2O]^{2+}$ layer ranging from ∼0.3 Å at 12 K to ∼0.2 Å at 295 K, corresponding to Mn−O−Mn bond angles of ∼163° and 168°. In order to clarify the trends observed in the thermal expansions of these three materials $(La_{2/3}Nd_{1/3})_2O_2Mn_2OSe_2$ was prepared; where the average radius of the *A* site was equal to that of Ce^{3+}. Analysis of the room temperature and 12 K unit cells for this material gave a_{12}/a_{300}, c_{12}/c_{300} and V_{12}/V_{300} ratios of 0.99759(4), 0.99603(6) and 0.99124(8), respectively. Comparison of these values with those in Figure 4 suggests that this material undergoes a similar thermal expansion to $La_2O_2Mn_2OSe_2$, and therefore suggests that the apparent behavior of the less pure $Ce_2O_2Mn_2OSe_2$ is anomalous.

Close inspection of the neutron diffraction data collected at 12 K for $La_2O_2Mn_2OSe_2$ shows the presence of two weak additional peaks at *d* = 1.68 and 1.70 Å, shown in Figure 5a. The intensity of these peaks is around 0.4% of the most intense reflection, the (015) at *d* = 2.78 Å. They are visible in both X-ray

dx.doi.org/10.1021/cm1035453 |*Chem. Mater.* 2011, 23, 1625–1635

Table 3. Selected Interatomic Distances and Bond Angles for $A_2O_2M_2OSe_2$ Materials at 12 K

		$La_2O_2Mn_2OSe_2$	$Ce_2O_2Mn_2OSe_2$	$Pr_2O_2Mn_2OSe_2$	$La_2O_2Fe_2OSe_2$[11]	$La_2O_2Co_2OSe_2$
bond lengths (Å)	d_{M-M}	2.91943(1)	2.90089(1)	2.89219(1)	2.88198(1)	2.8708(2)
	d_{M-O}	2.06435(1)	2.05124(1)	2.04709(1)	2.03786(1)	2.0300(1)
				2.04308(1)		
	d_{M-Se}	2.7908(2)	2.7871(3)	2.7807(4)	2.7080(3)	2.6794(7)
				2.7837(4)		
	d_{A-O}	2.3846(1)	2.3655(2)	2.331(2)	2.3764(2)	2.3727(5)
				2.357(2)		
	d_{A-Se}	3.3406(2)	3.3179(3)	3.3084(4)	3.3102(3)	3.2949(8)
bond angles (deg)	$M-Se-M$ (1)	63.074(6)	62.720(8)	62.63(1)	64.298(7)	64.79(2)
	$M-Se-M$ (2)	95.41(1)	94.78(1)	94.57(2)	97.62(1)	98.51(4)
				94.68(2)		
	$Se-M-Se$	84.59(1)	85.22(1)	85.43(2)	82.38(1)	81.49(4)
				85.32(2)		
	$A-O-A$ (1)	104.511(5)	104.362(8)	103.81(1)	105.346(7)	105.55(2)
	$A-O-A$ (2)	119.93(1)	120.26(2)	122.4(1)	118.08(2)	117.64(4)
				120.6(1)		

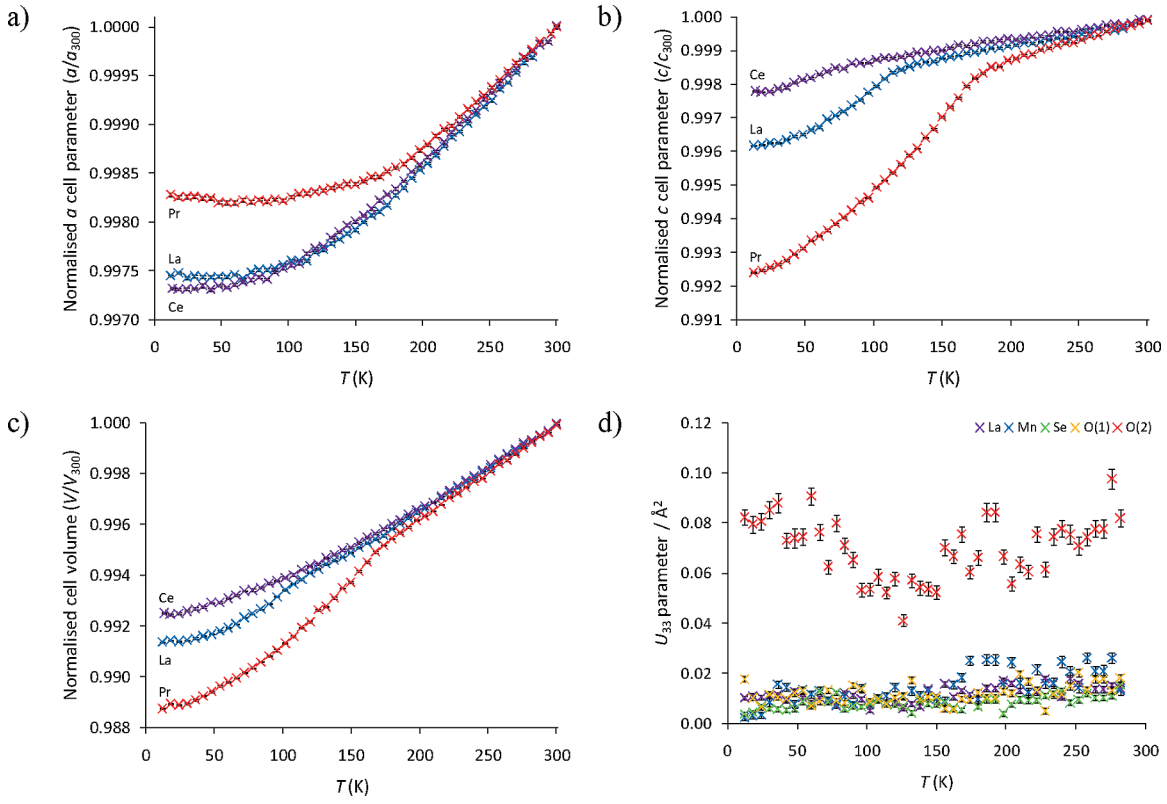

Figure 4. Effect of temperature on the (a) *a* cell parameters, (b) *c* cell parameters, and (c) volume for $A_2O_2Mn_2OSe_2$ and (d) U_{33} parameters for $La_2O_2Mn_2OSe_2$ (a similar plot for $Pr_2O_2Mn_2OSe_2$ is given in the Supporting Information); in (a) we plot $\sqrt{(ab)}$ for $Pr_2O_2Mn_2OSe_2$ at low temperature.

and neutron data suggesting that they are of structural, not magnetic, origin. Figure 5b shows how the intensity of these peaks changes as a function of temperature. Although the data quality from the rapid data sets collected on warming is relatively low, the data have been fitted using the expression $I_{calc} = I_0 \times (1 - (T/T_c))^{\beta}$, giving a T_c^{peaks} of 106(1) K and $\beta = 0.3(1)$. Although the appearance of these peaks is not exactly coincident with the discontinuities observed for the *c* cell parameter ($T_c = 115$ K) and O(2) U_{33} parameter, they are presumably indicative of ordering of the O(2) ions; the discrepancy in the critical temperatures for the different observations could arise from the relatively low intensity of the peaks and data quality available. We have been unable to index these peaks to a commensurate supercell. Similar peaks are also observed in the Pr^{3+} ($T_c^{peaks} = 170(1)$ K) but not the Ce^{3+} containing material, perhaps reflecting the smaller value of the O(2) U_{33} parameter in $Ce_2O_2Mn_2OSe_2$ (1.77×10^{-2}

dx.doi.org/10.1021/cm1035453 |*Chem. Mater.* 2011, 23, 1625–1635

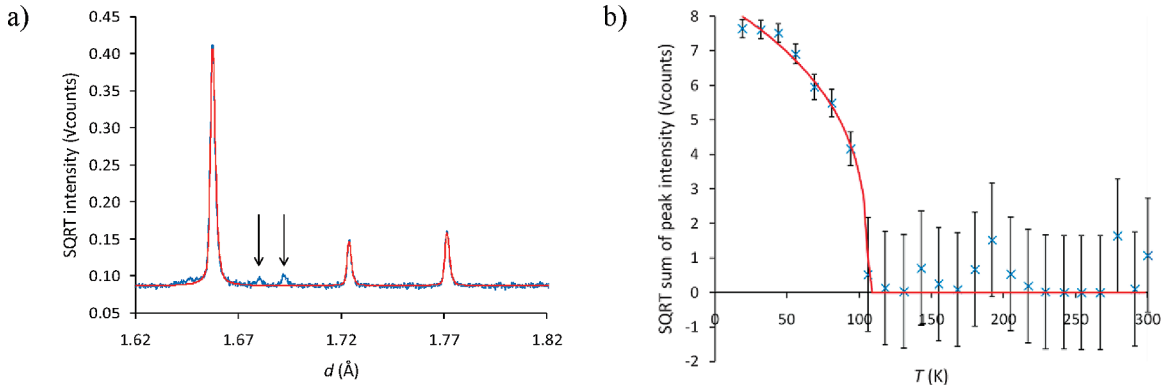

Figure 5. (a) Rietveld refinement of the nuclear plus magnetic model of $La_2O_2Mn_2OSe_2$ at 12 K between 1.62−1.82 Å and (b) the effect of temperature on the square root of the sum of the intensity of the peaks observed at 1.68 and 1.69 Å (similar plots for $Pr_2O_2Mn_2OSe_2$ are given in the Supporting Information); in both figures observed data are shown in blue and calculated in red; the solid guide line in (b) was fitted using the equation $I_{calcd} = I_0 \times (1 - (T/T_c^{peaks}))^{\beta}$.

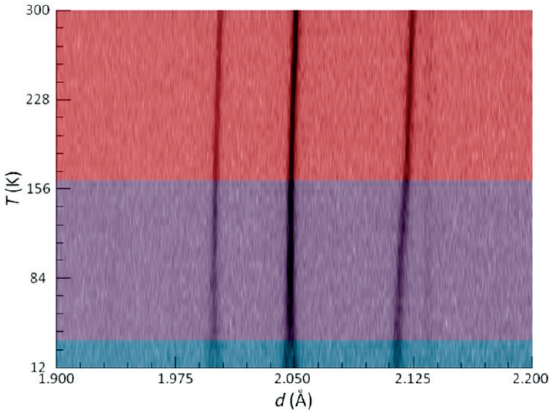

Figure 6. Pseudofilm plot showing the effect of temperature on the splitting of the 020 and 200 reflections at ∼2.05 Å; red = tetragonal, purple = peak broadening, blue = orthorhombic regions; plot shows the 1.9−2.2 Å (91−106 ms) region of the HRPD bs bank.

compared with 2.41×10^{-2} and 4.61×10^{-2} Å^2 for $La_2O_2Mn_2OSe_2$ and $Pr_2O_2Mn_2OSe_2$, respectively) and the less marked contraction of *c*. Oxide ion displacements have been reported in oxychalcogenide systems such as $Ba_2ZnO_2Ag_2Se_2$; however, these occur within the $[ZnO_2]^{2-}$ planes producing discrete ZnO_2 fragments.[34] The magnitude of U_{33} suggests displacements perpendicular to the layers in these materials.

Variable- temperature neutron diffraction data for $La_2O_2Mn_2OSe_2$ and $Ce_2O_2Mn_2OSe_2$ (Figure 4a) show no other significant changes on cooling apart from the magnetic ordering discussed below. $Pr_2O_2Mn_2OSe_2$, however (Figures 6 and 7a), shows a small but significant splitting of the 020 reflection on cooling below 36 K. This peak splitting can be modeled by a reduction in symmetry from tetragonal (*I*4/*mmm*) to orthorhombic (*Immm*), with an *a*/*b* ratio of 0.99804(1) at 12 K. This splitting is similar to that observed in PrOMnSb, which undergoes a reduction in symmetry from *P*4/*nmm* to *Pmmn* at 35 K, with an *a*/*b* ratio of ∼0.9957.[35] This transition is thought to be driven by local distortion of the Pr^{3+} ion symmetry and involves a reduction in point symmetry of the Pr^{3+} site from 4*mm* to *mm*2. Whereas in PrOMnSb, this transition is accompanied by magnetic ordering of the Pr^{3+} ions, no such ordering has been observed in $Pr_2O_2Mn_2OSe_2$ (Figure 11b). Similar investigations on $Pr_2O_2Fe_2OSe_2$ did not reveal any transition to a lower symmetry cell. Closer inspection of the neutron data shows that there is a gradual broadening of peaks from 180 K (i.e., coincident with the transition observed in the *c* axis), Figure 7b, presumably due to strain within the $[Pr_2O_2]^{2+}$ layers. This peak broadening continues until 36 K, at which point peak splitting is observed and the strain broadening becomes constant.

RESISTIVITY MEASUREMENTS

Resistivity data for $La_2O_2Mn_2OSe_2$ and $La_2O_2Co_2OSe_2$ are shown in Figure 8. Room temperature resistivities are 3.65×10^4 and 2.24×10^7 Ωcm respectively. A plot of $ln\rho$ against $1/T$ (Figure 8 inset) for each material gives a straight line, indicating semiconducting behavior; sample resistivities were too high to measure below 115 and 210 K for $La_2O_2Mn_2OSe_2$ and $La_2O_2Co_2OSe_2$ respectively. Activation energies for $La_2O_2Mn_2OSe_2$ and $La_2O_2Co_2OSe_2$ are calculated as 0.24 and 0.35 eV. Optical band gaps of 2.01 and 1.6(1) eV have been reported for $CeOMn_{0.5}Se$ and β-$La_2O_2MnSe_2$, respectively.[14,36] Results for $La_2O_2Co_2OSe_2$ are in agreement with resistivity studies by Wang et al.[19] The larger band gap in the cobalt-containing material is consistent with a change in sample color from olive green in $La_2O_2Mn_2OSe_2$ to light gray in $La_2O_2Co_2OSe_2$.

MAGNETIC PROPERTIES

On cooling $La_2O_2Mn_2OSe_2$ below ∼168 K extra peaks became visible in the neutron diffraction data (e.g., at 4.04 Å), whereas the intensity of other peaks (e.g., 3.45 Å) was seen to increase significantly (Figure 9a). These observations are consistent with antiferromagnetic (AFM) ordering of the Mn^{2+} ions, with k-vector of $\boldsymbol{k} = (0, 0, 0)$. Possible magnetic structures were investigated using SARAh Refine, interfaced with the GSAS software suite.[25,26] Results from this analysis suggested an AFM1 checkerboard arrangement of moments with moments along the *c*-axis (Figure 10a), which is described by a basis vector which transforms as the Γ_7 irreducible representation. This arrangement was modeled in TOPAS Academic using the *I*4′/*mm*′*m* Shubnikov group (labeled 139.534), and gave a refined Mn^{2+} moment of 4.223(7) μ_B at 12 K (see Table 2). The Mn^{2+} moment in $La_2O_2Mn_2OSe_2$ extracted from variable temperature data is shown in Figure 9b, where the solid line is a fitted using the equation $M_{calc} = M_0 \times (1 - (T/T_N))^{\beta}$, with $M_0 = 4.5(3)$ μ_B,

dx.doi.org/10.1021/cm1035453 |*Chem. Mater.* 2011, 23, 1625–1635

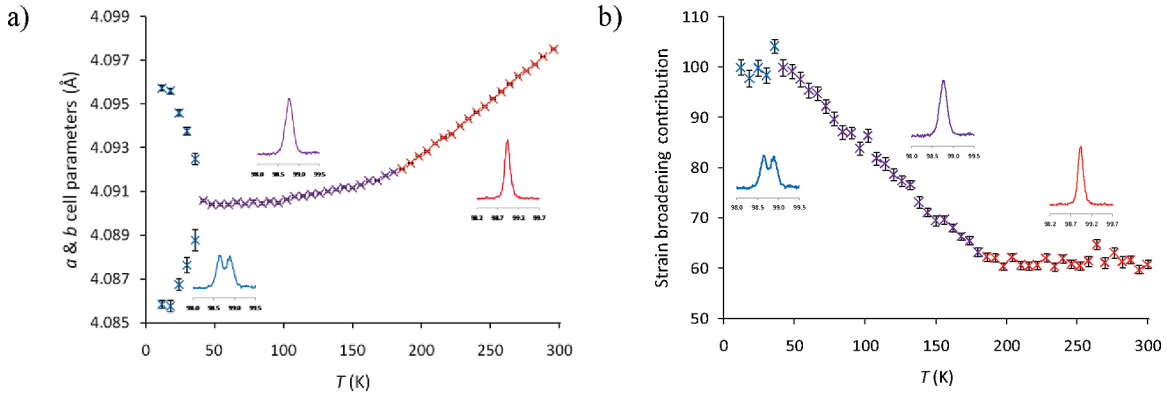

Figure 7. (a) *a* and *b* cell parameters for $Pr_2O_2Mn_2OSe_2$ as a function of temperature, with the 020 and 200 reflections at representative temperatures shown as insets and (b) the strain broadening contribution used to model the peak width; in both plots, red regions show the tetragonal regime, purple the peak broadening regime, and blue the orthorhombic.

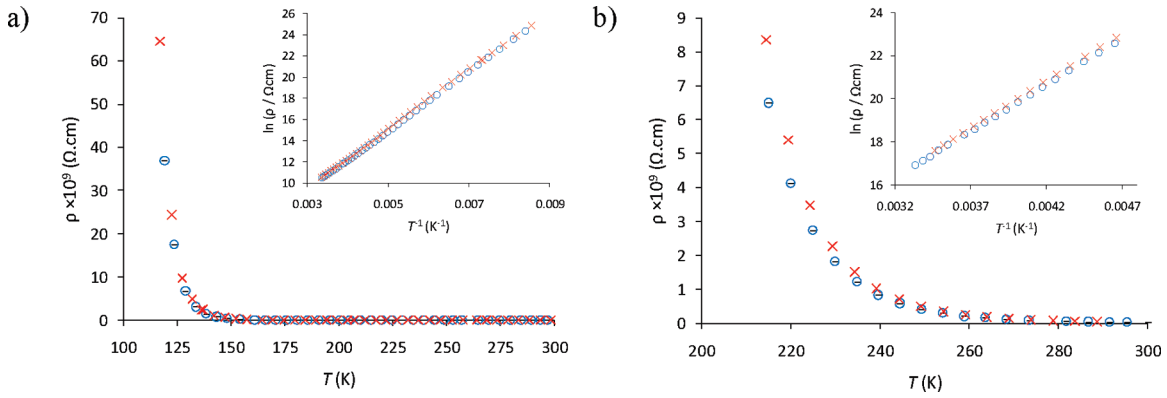

Figure 8. Temperature dependence of the resistivity of (a) $La_2O_2Mn_2OSe_2$ and (b) $La_2O_2Co_2OSe_2$ with Arrhenius plots of the data inset; cooling data are represented by blue circles and warming data by red crosses.

T_N = 168.1(4) K, and β = 0.24(7). Similar ordering was also observed in the cerium (M_0 = 4.8(3) μ_B, T_N = 174.1(2) K, and β = 0.29(7)) and praseodymium (M_0 = 4.5(1) μ_B, T_N = 180.3(4) K, and β = 0.27(4)) containing materials (see the Supporting Information). The increase observed for T_N is approximately linear with respect to decreasing rare-earth radius, probably due to increased overlap of the orbitals involved in magnetic coupling. For $Pr_2O_2Mn_2OSe_2$, due to the lowering of the nuclear symmetry, Shubnikov group $Im'm'm$ was used. M_z values for $Ce_2O_2Mn_2OSe_2$ and $Pr_2O_2Mn_2OSe_2$ at 12 K are 4.023(7) and 4.219(8) μ_B, respectively. These values are comparable to other Mn^{2+} containing materials, such as MnO (4.892 μ_B at 10 K) and Mn_2SiSe_4 (4.36(7) μ_B at 12 K).[37,38] There is no evidence for magnetic ordering of the rare-earth ions in either $Pr_2O_2Mn_2OSe_2$ or $Ce_2O_2Mn_2OSe_2$, over the temperature range studied from the current data. The arrangement of the Mn^{2+} ions is similar to that observed in PrOMnSb between 100 and 230 K.[35] On cooling PrOMnSb below 100 K the moments are observed to "flop" into the *ab* plane, with a 4 K moment on M_n of 3.69(3) μ_B.[35]

The arrangement of Mn^{2+} moments is discussed alongside other materials below, but is such that the nearest neighbor (Mn−Mn and 90° Mn−O−Mn), J_1 coupling interactions are all AFM, the ∼96° Mn−Se−Mn, J_2, interactions are a mixture of AFM and FM, and the 180° Mn−O−Mn, J_2', interactions are all FM. Although Goodenough's rules predict 180° cation−anion−cation exchange for d^5 ions to be strongly AFM, the structure adopted is dominated by the J_1 interactions.[39] Interestingly, independent theoretical studies calculated this AFM1 structure (Figure 10a) as one of the most stable configurations for both $La_2O_2Fe_2OSe_2$ and $B_2F_2Fe_2OQ_2$ (B = Sr, Ba; Q = S, Se), alongside the AFM6 structure.[12,40] There is no evidence to suggest the moments in the $A_2O_2Mn_2OSe_2$ materials order in an AFM6 arrangement, as no peaks relating to a $\boldsymbol{k}$ = (1/2, 0, 1/2) propagation vector are observed.

Susceptibility data for the three manganese-containing phases were recorded by SQUID magnetometery. As has been reported for several Mn-containing systems data have to be treated with caution as the presence of minor Mn-containing ferro- or ferrimagnetic impurities which are not visible by diffraction can dominate the data.[41] Magnetization versus applied field plots at 292 K were linear for all three materials with no hysteresis and an essentially zero intercept indicating paramagnetic behavior. Assuming μ_{eff} values for La, Pr and Ce of 0, 3.58 and 2.54 μ_B, respectively, Mn μ_{eff} values of 2.7, 2.5, and 2.5 μ_B were obtained from these data.

Figure 11 shows the molar susceptibility for $La_2O_2Mn_2OSe_2$ from field-cooled (FC) and zero-field cooled (ZFC) experiments in a 1000 Oe field. There is a significant divergence in FC/ZFC data at low temperature and marked discontinuities in the FC data at ∼40 and ∼140 K. FC and ZFC curves meet at around 167 K with a small discontinuity at this point. This is similar to the Néel temperature determined from neutron diffraction data (168 K), and represents AF ordering of Mn moments. Above this temperature susceptibility versus temperature has a positive

dx.doi.org/10.1021/cm1035453 |*Chem. Mater.* 2011, 23, 1625–1635

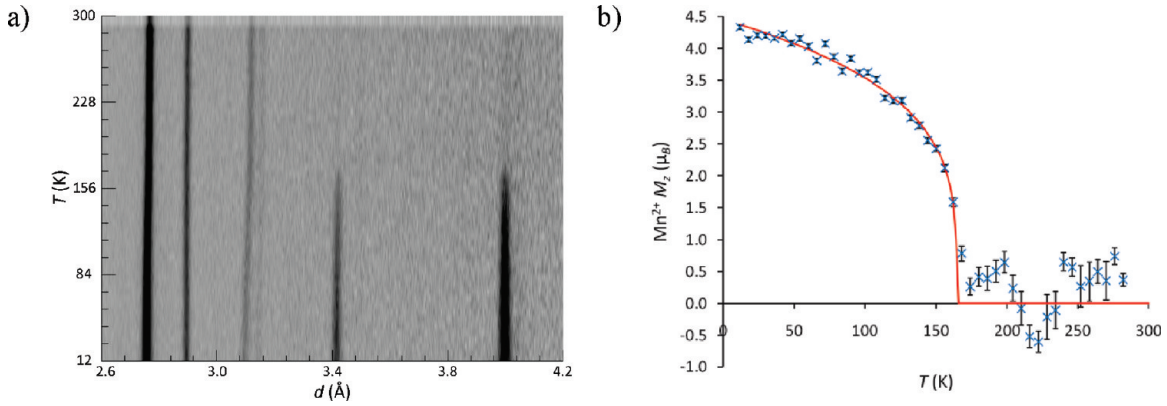

Figure 9. (a) Evolution of the observed magnetic peaks for $La_2O_2Mn_2OSe_2$ and (b) the magnitude of the Mn^{2+} moment in $La_2O_2Mn_2OSe_2$ as a function of temperature; the pseudofilm plot shows the 2.6−4.2 Å (90−146 ms) region of the 90° HRPD bank; the solid line in (b) is described in the text.

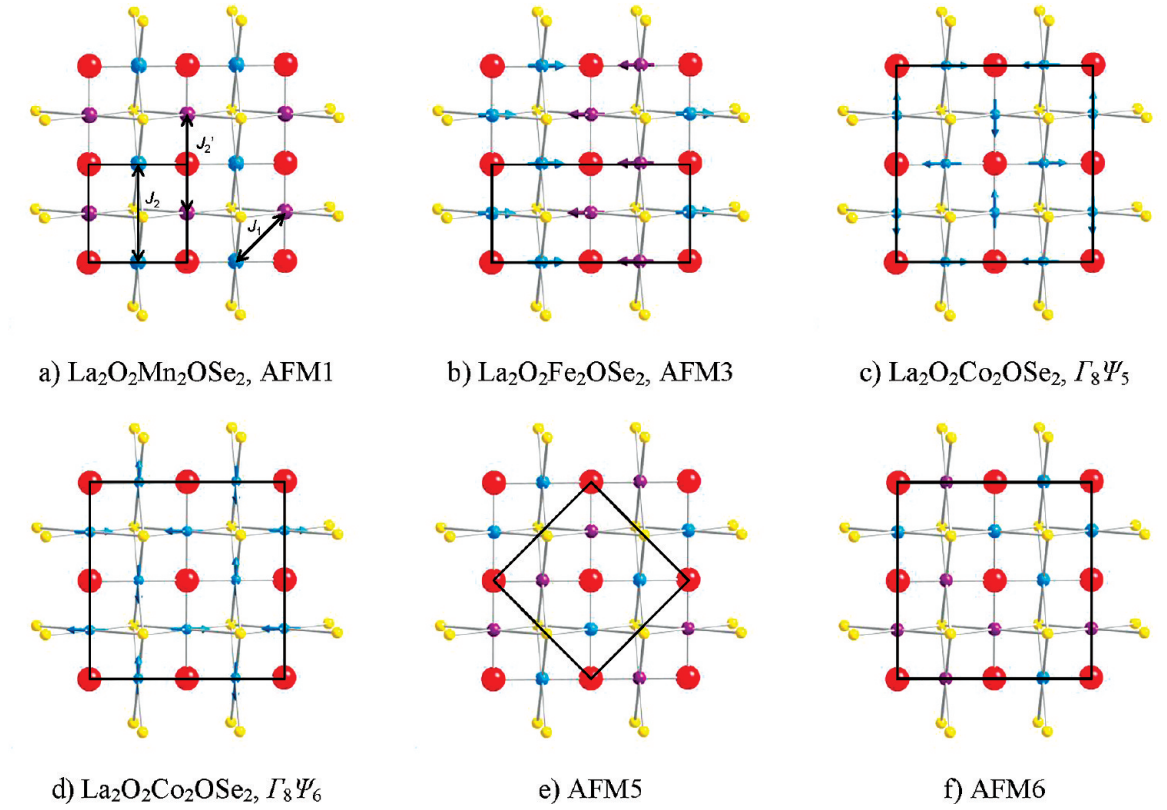

Figure 10. Observed and theoretical magnetic structures: (a) $La_2O_2Mn_2OSe_2$ (AFM1), (b) $La_2O_2Fe_2OSe_2$ (AFM3) and (c, d) $La_2O_2Co_2OSe_2$ $\Gamma_8\Psi_5$ & $\Gamma_8\Psi_6$, (e) AFM5 and (f) AFM6; O = red, Se = yellow, M^{2+} = blue/purple; for a, b, e, and f, the blue/purple color of the M^{2+} ions relates similarly orientated moments within each cell; the magnetic cells are outlined.

gradient, and the material shows non-Curie−Weiss behavior. Similar behavior is systems such as chromium metal, $Na_{0.5}CoO_2$, $LaO_{1-x}F_xFeAs$ and $La_2O_2Co_2OSe_2$.[19,42−44] It presumably reflects the presence of strong short-range AFM interactions in the sample well above T_N which also results in the low room temperature moment observed for Mn^{2+}. The presence of strong interactions well above T_N reflects the frustrated nature of the magnetic structure. The lack of changes in the neutron data below 168 K suggests that the low temperature features are not intrinsic to $La_2O_2Mn_2OSe_2$. We believe the features below 45 K are due to trace quantities of Mn_3O_4 which has T_N = 42 K. Superparamagnetic Mn_3O_4 nanoparticles have been shown to exhibit magnetic behavior similar to that in Figure 11, with blocking temperatures ∼40 K for 10 nm particles.[45,46] A <0.5% weight percent impurity would be sufficient to explain the behavior observed. Hysteresis loops at low temperature are also consistent with the presence of Mn_3O_4; a plot of magnetization versus applied field at 2 K is given as Supporting Information. The ∼140 K discontinuity could be due to smaller amounts of $LaMnO_3$. Nonstoichiometric $LaMnO_3$ orders ferromagnetically at 140 K and exhibits divergence between FC and ZFC data.[47,48] Both impurity phases would be difficult to detect from powder

dx.doi.org/10.1021/cm1035453 |Chem. Mater. 2011, 23, 1625–1635

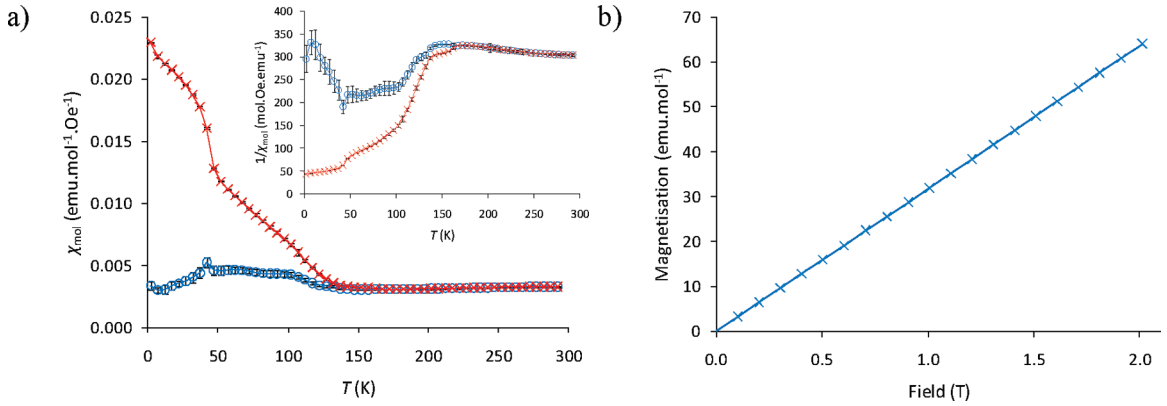

Figure 11. (a) Magnetic susceptibility as a function of temperature for FC and ZFC measurements for $La_2O_2Mn_2OSe_2$ (per mole of $LaOMnO_{0.5}Se$) and (b) magnetization as a function of field at room temperature; FC data are represented by red crosses and ZFC are blue circles, inset to (a) shows $1/\chi_{mol}$ versus T.

data, although small amounts of perovskite impurity have been observed in preparations of Fe^{2+} and Co^{2+} analogues. Variable temperature susceptibility data for A = Ce & Pr show no evidence for Pr^{3+} or Ce^{3+} ordering. After this work was completed two papers have appeared on the $La_2O_2Mn_2OSe_2$ system. Single crystal susceptibility measurements by Liu et al. suggest a small canting of Mn moments.[22] Ni et al have independently described the low T magnetic structure of $La_2O_2Mn_2OSe_2$.[23] Their data confirm short-range 2D magnetic order above T_N, consistent with the low Mn moment observed.

MAGNETIC ORDERING IN $La_2O_2Co_2OSe_2$

Our neutron diffraction studies of $La_2O_2Co_2OSe_2$ are consistent with those reported by Fuwa et al. as this work was being submitted, and showed the presence of several new peaks consistent with an enlarged unit cell with $\boldsymbol{k}$ = (1/2, 1/2, 0) at 200 K and below (this is consistent with AFM ordering with T_N = 220 K observed from susceptibility and heat capacity measurements).[17,19,20] Solutions of the 12 K structure were investigated using SARAh Refine which suggested two models described by basis vectors which transform as the Γ_8 irreducible representation: $\Gamma_8\Psi_5$ and $\Gamma_8\Psi_6$, which cannot be distinguished from powder data.[25] The corresponding structures are shown in Figure 10c, d, and contain moments directed either along, or perpendicular to, the Co−O bonds. These layers propagate in the c direction by a translation of (1/4, 1/4, 1/2). The former is equivalent to that proposed by Fuwa et al.[20] In both arrangements, the J_2 and J_2' interactions (the ∼99 °Co−Se−Co and 180 °Co−O−Co next nearest neighbor (n.n.n.) interactions, respectively) are AFM. The J_1 interactions (nearest neighbor (n.n.) 90 °Co−Co interactions), however, all have some degree of frustration, with the moments lying perpendicular to each other. While the observation of AFM ordering is consistent with susceptibility data, the arrangement adopted is different to that predicted from computational studies, which predicted an AFM6 structure with weakly FM J_2 interactions.[17,19,49] Final refinements of the magnetic structure were performed in GSAS using a nuclear-only phase in $I4/mmm$ and a magnetic-only phase in $P1$, although refinements in TA shows that the data could be equally well described using P_Cmmn Shubnikov symmetry in a cell of $\sqrt{2}a \times \sqrt{2}a$. Results from the final refinement in GSAS and Rietveld plots are given in Supporting Information. A refined moment of 3.29(3) μ_B for the Co^{2+} ion is consistent with high spin Co^{2+}, confirming suggestions by Wu, which argued against the low spin arrangement suggested by Wang et al., and similar to the 3.5 μ_B reported by Fuwa.[19,50]

DISCUSSION

Figure 10 summarizes the different magnetic structures adopted by the $La_2O_2M_2OSe_2$ materials as one crosses the periodic table, reflecting the changing balance of exchange interactions. There are three interactions to consider, the four J_1 n.n. interactions (direct $M-M$, 90° $M-O-M$, and ∼64° $M-Se-M$), two J_2 ∼95° nnn $M-Se-M$ interactions, and two J_2' 180° nnn $M-O-M$ interactions. We note that three different sets of labels have now been used in the literature for these interactions. We adopt those of Zhu et al., which are similar to those used in the iron pnictide literature.[12] Zhu et al. have calculated the T = 0 K phase diagram for a Heisenberg system with this arrangement, predicting the AFM1, AFM5 and AFM6 models in Figure 10 to be stable for different values of exchange interactions. Values of J_n/S^2 have been calculated for materials with $[Fe_2O]^{2+}$ ($La_2O_2Fe_2OSe_2$, $Ba_2Se_2Fe_2OF_2$, and $Sr_2S_2Fe_2OF_2$) and $[Co_2O]^{2+}$ ($La_2O_2Co_2OSe_2$) layers using GGA+U/LSDA+U, methods.[12,40,49] With U = 3 eV values of (J_1/S^2):(J_2/S^2):(J_2'/S^2) for $La_2O_2Fe_2OSe_2$ are −3.8:+1.1:−4.8, and for $La_2O_2Co_2OSe_2$ are −4.0:+0.8:−12.4 meV, a negative J representing AFM interactions. For the case where J_2 is small and positive (as expected from Goodenough-Kanemori rules[51,52]), the simple AFM1 checkerboard arrangement, Figure 10a, is predicted for $|J_2'| < |J_1|$ (labeled 2F3A by Kabbour), whereas for $|J_2'| > |J_1|$ the AFM6 arrangement, Figure 10f, is predicted (Kabbour's 1A2F).[40] Experimentally, we find that for M = Mn, the AFM1 structure is adopted at low temperatures with T_N increasing as cell parameter decreases. As such it appears that the J_1 interactions, which are calculated to be AFM for these materials, dominate. The J_2' Mn−O−Mn interactions, which one would predict to be AFM from the Goodenough−Kanamori rules, are fully frustrated.[51,52] As the transition metal electronegativity increases across the transition series one would anticipate the strength of these interactions would increase, and this is reflected computationally. Experimentally $La_2O_2Fe_2OSe_2$ adopts the fully frustrated structure (also observed for FeTe) shown in Figure 10b, in which half of the Fe−O−Fe interactions are satisfied and half frustrated.[11,21,53−55] In $La_2O_2Co_2OSe_2$, all the 180 °Co−O−Co antiferromagnetic interactions are satisfied. As shown by Wu's calculations, magnetic frustration is weaker in the Co system than in Fe. As the magnitude of U is changed from

dx.doi.org/10.1021/cm1035453 |Chem. Mater. 2011, 23, 1625–1635

2−4 eV $|J_2'|/|J_1|$ remains >3 for M = Co. For M = Fe $|J_2'|/|J_1|$ varies from 2.43 to 0.97 for U = 1.5−4.5 eV, and as such would cross the AFM1-AFM6 phase boundary. There is a tight balance between the various magnetic interactions which leads to the range of structures adopted. $M-M$ n.n. interactions reduce and 180° M-O-M interactions grow in importance as the electronegativity of the transition metal increase. Although we might expect exchange interactions to be influenced by ordering of the O atoms away from $[M_2O]^{2+}$ layers, for the Mn^{2+} materials, this does not appear to affect their magnetic structures.

CONCLUSIONS

We have successfully prepared seven new members of the $A_2O_2M_2OSe_2$ family of materials; $A_2O_2Fe_2OSe_2$ (A = Ce, Pr, Nd, Sm) and $A_2O_2Mn_2OSe_2$ (A = La, Ce, Pr). Further synthesis of analogous materials was unsuccessful, suggesting that this structure is stable for a restricted range of rare earth and transition metals. Variable temperature X-ray and neutron data have shown that the Mn^{2+} series of materials undergo a structural distortion on cooling, most noticeable in the c lattice parameter, thought to coincide with the static displacement of the O(2) ions out of the square planar $[Mn_2O]^{2+}$ layer. This effect is most pronounced in the Pr^{3+} containing material, reflecting the shorter Mn−O bond involved. X-ray and neutron diffraction data show the appearance of weak superstructure peaks in the lanthanum and praseodymium containing materials that are presumably related to O(2) ordering. We have also demonstrated that $Pr_2O_2Mn_2OSe_2$, like PrOMnSb, undergoes a symmetry-reducing phase transition on cooling below 36 K, involving local distortion of the Pr^{3+} ion.

Neutron diffraction data have shown that the Mn series of materials order with an AFM1 structure at low temperature, with $T_N \approx 170$ K, different from that observed for $La_2O_2Fe_2OSe_2$ and $La_2O_2Co_2OSe_2$. The observation of antiferromagnetic ordering is in agreement with magnetic susceptibility measurements. We have also reported the magnetic structure of $La_2O_2Co_2OSe_2$, and demonstrated the ordering to be different to that predicted by Wu.[49]

ASSOCIATED CONTENT

Supporting Information. Additional tables and figures (PDF). This material is available free of charge via the Internet at http://pubs.acs.org.

AUTHOR INFORMATION

Corresponding Author
*E-mail: john.evans@durham.ac.uk.

ACKNOWLEDGMENT

We thank A. Daoud-Aladine (ISIS) and R. Ibberson (ISIS) for measurements on HRPD at the ISIS facility, I. Terry (Durham) and K. Prassides (Durham) for MPMS measurements, A. Brinkman and R. Schmidt (Durham) for resistivity measurements, and EPRSC (EP/F066422/1) for funding.

REFERENCES

(1) de la Cruz, C.; Huang, Q.; Lynn, J. W.; Li, J.; Ratcliff, W., II; Zarestky, J. L.; Mook, H. A.; Chen, G. F.; Luo, J. L.; Wang, N. L.; Dai, P. *Nature* **2008**, *453*, 899–902.
(2) Kamihara, Y.; Hiramatsu, H.; Hirano, M.; Kawamura, K.; Yanagi, H.; Kamiya, T.; Hosono, H. *J. Am. Chem. Soc.* **2006**, *128*, 10012–10013.
(3) Wen, H.-H.; Mu, G.; Fang, L.; Yang, H.; Zhu, X. *Europhys. Lett.* **2008**, *82*, 17009.
(4) Hsu, F. C.; Luo, J. Y.; Yeh, K. W.; Chen, T. K.; Huang, T. W.; Wu, P. M.; Lee, Y. C.; Huang, Y. L.; Chu, Y. Y.; Yan, D. C.; Wu, M. K. *P. Natl. Acad. Sci. USA* **2008**, *105*, 14262–14264.
(5) Li, Z.; Ju, J.; Tang, J.; Sato, K.; Watahiki, M.; Tanigaki, K. *J. Phys. Chem. Solids* **2010**, *71*, 495–498.
(6) Margadonna, S.; Takabayashi, Y.; McDonald, M. T.; Kasperkiewicz, K.; Mizuguchi, Y.; Takano, Y.; Fitch, A. N.; Suard, E.; Prassides, K. *Chem. Commun.* **2008**, 5607–5609.
(7) Paglione, J.; Greene, R. L. *Nat Phys* **2010**, *6*, 645–658.
(8) Ozawa, T. C.; Kauzlarich, S. M. *Sci. Technol. Adv. Mater.* **2008**, *9*, 033003.
(9) Johnston, D. C. *Adv. Phys.* **2010**, *59*, 803–1061.
(10) Mayer, J. M.; Schneemeyer, L. F.; Siegrist, T.; Waszczak, J. V.; Dover, B. v. *Angew. Chem., Int. Ed. Engl.* **1992**, *31*, 1645–1647.
(11) Free, D. G.; Evans, J. S. O. *Phys. Rev. B* **2010**, *81*, 214433.
(12) Zhu, J. X.; Yu, R.; Wang, H.; Zhao, L. L.; Jones, M. D.; Dai, J.; Abrahams, E.; Morosan, E.; Fang, M.; Si, Q. *Phys. Rev. Lett.* **2010**, *104*, 216405.
(13) Pottgen, R.; Johrendt, D. *Z. Naturforsch.* **2008**, *63b*, 1135–1148.
(14) Ijjaali, I.; Mitchell, K.; Haynes, C. L.; McFarland, A. D.; van Duyne, R. P.; Ibers, J. A. *J. Solid State Chem.* **2003**, *176*, 170–174.
(15) McCabe, E. E.; Free, D. G.; Evans, J. S. O. *Chem. Commun.* **2011**, *47*, 1261–1263.
(16) Hiramatsu, H.; Ueda, K.; Kamiya, T.; Ohta, H.; Hirano, M.; Hosono, H. *J. Phys. Chem. B* **2004**, *108*, 17344–17351.
(17) Fuwa, Y.; Wakeshima, M.; Hinatsu, Y. *Solid State Commun.* **2010**, *150*, 1698–1701.
(18) Liu, R. H.; Song, Y. A.; Li, Q. J.; Ying, J. J.; Yan, Y. J.; He, Y.; Chen, X. H. *Chem. Mater.* **2010**, *22*, 1503–1508.
(19) Wang, C.; Tan, M.-q.; Feng, C.-m.; Ma, Z.-f.; Jiang, S.; Xu, Z.-a.; Cao, G.-h.; Matsubayashi, K.; Uwatoko, Y. *J. Am. Chem. Soc.* **2010**, *132*, 7069–7073.
(20) Fuwa, Y.; Wakeshima, M.; Hinatsu, Y. *J. Phys.: Condens. Matter* **2010**, *22*, 346003.
(21) Li, S.; de la Cruz, C.; Huang, F. Q.; Chen, Y.; Lynn, J. W.; Hu, J.; Huang, Y. L.; Hsu, F. C.; Yeh, K. W.; Wu, M. K.; Dai, P. *Phys. Rev. B* **2009**, *79*, 054503.
(22) Liu, R. H.; Zhang, J. S.; Cheng, P.; Luo, X. G.; Chen, X. H. arXiv:1011.6053v1 2010.
(23) Ni, N.; Climent-Pascual, E.; Jia, S.; Huang, Q.; Cava, R. J. *Phys. Rev. B* **2010**, *82*, 214419.
(24) Coelho, A. A. *TOPAS Academic: General Profile and Structure Analysis Software for Powder Diffraction Data, 5*; Bruker AXS: Karlsruhe, Germany, 2010.
(25) Wills, A. S. *Physica B* **2000**, *276−278*, 680–681.
(26) Larson, A. C.; Von Dreele, R. B. *The General Structure Analysis System (GSAS)*; Los Alamos National Laboratory: Los Alamos, NM, 2004.
(27) Shannon, R. D. *Acta Crystallogr., Sect. A* **1976**, *32*, 751–767.
(28) Ohtani, T.; Hirose, M.; Sato, T.; Nagaoka, K.; Iwabe, M. *Jpn. J. Appl. Phys.* **1993**, *32* (Suppl. 32−3), 316–318.
(29) Charkin, D. O.; Akopyan, A. V.; Dolgikh, V. A. *Russ. J. Inorg. Chem.* **1999**, *44*, 833–837.
(30) Schob, O.; Parthe, E. *Acta Crystallogr.* **1965**, *19*, 214–224.
(31) Chan, G. H.; Deng, B.; Bertoni, M. I.; Ireland, J. R.; Hersam, M. C.; Mason, T. O.; Duyne, R. P. v.; Ibers, J. A. *Inorg. Chem.* **2006**, *45*, 8264–8272.
(32) Pitcher, M. J.; Smura, C. F.; Clarke, S. J. *Inorg. Chem.* **2009**, *48* 9054–9056.
(33) Ueda, K.; Takafuji, K.; Hosono, H. *J. Solid State Chem.* **2003**, *170*, 182–187.
(34) Herkelrath, S. J. C.; Saratovsky, I.; Haderman, J.; Clarke, S. J. *J. Am. Chem. Soc.* **2008**, *130*, 14426–14427.
(35) Kimber, S. A. J.; Hill, A. H.; Zhong-Zhang, Y.; Jeschke, H. O.; Valenti, R.; Ritter, C.; Schellenberg, I.; Hermes, W.; Pottgen, R.; Argyriou, D. N. *Phys. Rev. B* **2010**, *82*, 100412.

(36) McCabe, E. E.; Free, D. G.; Mendis, B.; Higgins, J.; Evans, J. S. O. *Chem. Mater.* **2010**, *22*, 6171–6182.
(37) Bonfante, M.; Moussa, F.; Hennion, B.; Pepy, G. *Solid State Commun.* **1972**, *10*, 553-&.
(38) Bodenan, F.; Cajipe, V. B.; Ouvard, G.; André, G. *J. Magnetism and Magnet. Mater.* **1996**, *164*, 233–240.
(39) Goodenough, J. B. *Magnetism and the Chemical Bond*, 1st ed.; John Wiley & Sons: New York, 1963.
(40) Kabbour, H.; Janod, E.; Corraze, B.; Danot, M.; Lee, C.; Whangbo, M.-H.; Cario, L. *J. Am. Chem. Soc.* **2008**, *130*, 8261–8270.
(41) Goff, R. J.; Williams, A. J.; Attfield, J. P. *Phys. Rev. B* **2004**, *70*, 014426.
(42) Pepper, A. R.; Street, R. *Proc. Phys. Soc.* **1966**, *87*, 971–973.
(43) Viciu, L.; Bos, J. W. G.; Zandbergen, H. W.; Huang, Q.; Foo, M. L.; Ishiwata, S.; Ramierz, A. P.; Lee, M.; Ong, N. P.; Cava, R. J. *Phys. Rev. B* **2006**, *73*, 174104.
(44) Klingeler, R.; Leps, N.; Hellmann, I.; Popa, A.; Stockert, U.; Hess, C.; Kataev, V.; Grafe, H. J.; Hammerath, F.; Lang, G.; Wurmehl, S.; Behr, G.; Harnagea, L.; Singh, S.; Büchner, B. *Phys. Rev. B* **2010**, *81*, 024506.
(45) Seo, W. S.; Jo, H. H.; Lee, K.; Kim, B.; Oh, S. J.; Park, J. T. *Angew. Chem., Int. Ed.* **2004**, *43*, 1115–1117.
(46) Regmi, R.; Tackett, R.; Lawes, G. *J. Magn. Magn. Mater.* **2009**, *321*, 2296–2299.
(47) Ghivelder, L.; Abrego Castillo, I.; Gusm; atilde; o, M. A.; Alonso, J. A.; Cohen, L. F. *Phys. Rev. B* **1999**, *60*, 12184.
(48) Huang, Q.; Santoro, A.; Lynn, J. W.; Erwin, R. W.; Borchers, J. A.; Peng, J. L.; Greene, R. L. *Phys. Rev. B* **1997**, *55*, 14987–14999.
(49) Wu, H. *Phys. Rev. B* **2010**, *82*, 020410.
(50) Withers, N. D. Ph.D., Durham University, Durham, U.K., 2005.
(51) Goodenough, J. B. *Phys. Rev.* **1955**, *100*, 564.
(52) Kanamori, J. *J. Phys. Chem. Solids* **1959**, *10*, 87–98.
(53) Fruchart, D.; Convert, P.; Wolfers, P.; Madar, R.; Senateur, J. P.; Fruchart, R. *Mater. Res. Bull.* **1975**, *10*, 169–174.
(54) Bao, W.; Qui, Y.; Huang, Q.; Green, M. A.; Zajdel, P.; Fitzsimmons, M. R.; Zhernenkov, M.; Chang, S.; Fang, M.; Qian, B.; Vehstedt, E. K.; Yang, J.; Pham, H. M.; Spinu, L.; Mao, Z. Q. *Phys. Rev. Lett.* **2009**, *102*, 241001.
(55) Fang, C.; Bernevig, B. A.; Hu, J. *Europhys. Lett.* **2009**, *86*, 67005.